Extended Abstract, 38th Conference on Radar Meteorology, AMS, Chicago, IL, 28 August - 1 September 2017

# P49 ASSESSING ESTIMATES OF LOW-LEVEL SUPERCELL CIRCULATION AND AREAL EXPANSION RATE DIAGNOSED FROM DOPPLER RADAR DATA: SIMULATION STUDY

Vincent T. Wood[2], Robert P. Davies-Jones[1,2], and Corey K. Potvin[2,3,4]
[1]Emeritus, [2]NOAA/OAR/National Severe Storms Laboratory,
[3]Cooperative Institute for Mesoscale Meteorological Studies, and
[4]School of Meteorology, University of Oklahoma,
Norman, Oklahoma, USA

## 1. INTRODUCTION

Wood and Davies-Jones (2015) simulated Doppler velocity fields that a Doppler radar would see as it scanned an axisymmetric vortex embedded in a convergent axisymmetric flow. We gauged the detection and measurement of significant circulation around and areal expansion rate of a curve as a method for giving advanced warnings of tornadoes. Circulation (rate of areal expansion) is the line integral around a closed curve of velocity tangential (outward normal) to the curve. Circulation and areal expansion rate (the negative of areal contraction rate) may be more useful than differential single-Doppler velocities in the characteristic velocity couplet for detecting and measuring the strength of convergent tornadic mesocyclones at low altitudes. This is because circulation and areal expansion rate are (a) less scale dependent, (b) more tolerant of noisy Doppler velocity data, and (c) relatively insensitive to range and azimuth, beamwidth and location of a tornado within a sampling volume.

The objective of the paper is to investigate and assess estimates of simulated low-level supercell circulation and areal contraction rate diagnosed from virtual Doppler radar vortex signatures of two simulated tornadoes. Wood and Davies-Jones (2015) derived three-dimensional velocity components of radar targets, as will be presented in section 2. Circulation and areal expansion rate formulas derived by Wood and Davies-Jones (2015) are discussed in sections 3 and 4. Section 5 briefly describes a "truth" tornadic supercell simulation using a high-resolution cloud model. The numerical model results will be used to compare and verify the simulated single-Doppler circulation and areal expansion rate values.

## 2. THREE-DIMENSIONAL VELOCITY COMPONENTS OF RADAR TARGETS

Since a Doppler radar scans the 3D velocity components of a target within a volume scan, it is expeditious and computationally economical to determine the kinematic properties of the velocity field in the conical surfaces of constant elevation angle. Following the approach of Doviak and Zrnić (1993), we define a radar spherical, right-handed coordinate system ($R$, $\alpha$, $\beta$) centered on the radar where $R$ is the slant range, $\alpha$ is the elevation angle measured upward from the horizon, and $\beta$ is the azimuth angle measured clockwise from due north (Fig. 1). The surface of constant elevation angle $\alpha_o$ is called henceforth the $\alpha_o$-surface. In terms of Cartesian coordinates ($x$, $y$, $z$) where the radar is at the origin, the positive $x$- and $y$-axes are, respectively, directed towards the east and north in the plane tangent to the earth's surface and the $z$-axis points towards the zenith. The corresponding unit basis vectors are $\mathbf{i}$, $\mathbf{j}$, and $\mathbf{k}$, respectively. The radar target's positions owing to the earth's curvature are given in a matrix form as (Wood and Davies-Jones 2015)

$$\mathbf{R} \equiv \begin{bmatrix} x \\ y \\ z \end{bmatrix} = \begin{bmatrix} R\cos\alpha\sin\beta \\ R\cos\alpha\cos\beta \\ R\sin\alpha \end{bmatrix}, \qquad (2.1)$$

where the spherical coordinates are related to the Cartesian coordinates by $R = |\mathbf{R}| = \sqrt{x^2 + y^2 + z^2}$, $\alpha = \sin^{-1}(z/R)$, and $\beta = \tan^{-1}(x/y)$. Since Eq. (2.1) does not include the corrected elevation angle ($\alpha_o'$) that represents the sum of the radar beam's elevation angle ($\alpha_o$) to the data point and the angle subtended by the verticals at the radar and at the measurement (i.e., data) point, we follow Doviak and Zrnić (1993) who replace $\alpha$ in Eq. (2.1) with the corrected elevation angle $\alpha_o'$, where $\alpha_o' = \alpha_o + \tan^{-1}[R\cos\alpha_o/(a_e + R\sin\alpha_o)]$. The variable $a_e = k_e a$ represents the effective radius of earth; $a = 6371$ km is the mean radius of earth; and $k_e = 1.21$.

Wood and Davies-Jones (2015) showed that a 3D vector velocity $\mathbf{V}$ of the targets is obtained by replacing $\alpha$ in (2.1) with $\alpha_o'$ and then differentiating with respect to time $t$

$$\mathbf{V} = V_R\widehat{\mathbf{R}} + V_\alpha\widehat{\boldsymbol{\alpha}} + V_\beta\widehat{\boldsymbol{\beta}}, \qquad (2.2)$$

where $R_t \equiv \frac{dR}{dt}$, $\alpha_t \equiv \frac{d\alpha_o'}{dt}$, $\beta_t \equiv \frac{d\beta}{dt}$, $V_R = R_t$, $V_{\alpha_o'} = R\alpha_t$, and $V_\beta = R\cos\alpha_o'\,\beta_t$. Here, $\widehat{\mathbf{R}}$ is in the direction of increasing slant range, $\widehat{\boldsymbol{\alpha}}$ is in the direction of increasing elevation angle, and $\widehat{\boldsymbol{\beta}}$ is in the direction of increasing azimuth. The first component $V_R$ is the observed Doppler velocity component. The other components $V_\alpha$ and $V_\beta$ are unobserved because they are perpendicular to the radar viewing direction. In the formulas derived below, the observed parts of the quantities are obtained by setting the unobserved velocity components to zero (i.e., ignoring them).

## 3. CIRCULATION AND VORTICITY

By Stokes' theorem, the relationship between circulation and vorticity is given by

$$\Gamma = \oint_C \mathbf{V} \cdot d\boldsymbol{\tau} = \iint_A (\boldsymbol{\omega} \cdot \mathbf{n})\, dA \ , \qquad (3.1)$$

Here, the circulation $\Gamma$ about a closed circuit $C$ is defined as the line integral about the circuit of the tangential component of vector velocity $\mathbf{V}$ and is equivalent to the integral over the corresponding area $A$ of the component of vector vorticity $\boldsymbol{\omega}(= \boldsymbol{\nabla} \times \mathbf{V})$ normal to the surface. The line element $d\boldsymbol{\tau}$ is the unit vector tangent to the curve in the counterclockwise direction; $\mathbf{n}$ is an outward-pointing unit normal vector to the surface.

In the radar spherical coordinate system, the relative vorticity normal to the $\alpha_o'$-surface is given by

$$\omega_\alpha \equiv (\nabla \times \mathbf{V}) \cdot \hat{\boldsymbol{\alpha}} = \frac{1}{R\cos\ \alpha_o'}\frac{\partial V_R}{\partial \beta} - \frac{1}{R}\frac{\partial}{\partial R}\left(RV_\beta\right) \ . \quad (3.2)$$

The minus sign in (3.2) arises because $\beta$ increases in the clockwise direction. The term $\frac{1}{R\cos\ \alpha_o'}\frac{\partial V_R}{\partial \beta} - \frac{\partial V_\beta}{\partial R}$ represents the shear vorticity of the radar's target; $-\frac{V_\beta}{R}$ is the curvature vorticity. The circulation $\Gamma$ around the boundary $C$ of an area $A$ in the $\alpha_o'$-surface is obtained from (3.1) and (3.2), via Stokes' theorem, as follows:

$$\begin{aligned}\Gamma &= \cos\alpha_o' \iint_A \omega_\alpha R dR d\beta \\ &= \iint_A \frac{\partial V_R}{\partial \beta} d\beta dR - \cos\alpha_o' \iint_A \frac{\partial}{\partial R}(RV_R) dR d\beta \ , \quad (3.3) \\ &= \oint_C (V_R dR + V_\beta R\cos\alpha_o'\, d\beta) \ .\end{aligned}$$

The mean vorticity in $A$ in the direction perpendicular to the $\alpha_o'$-surface is $\Gamma/A$. Multiplying this quantity by $\cos\alpha_o'$ gives its contribution to the mean vertical vorticity $\overline{\zeta}$ in $A$.

By ignoring $V_\beta$ in (4.3), we obtain the observed circulation $\Gamma_{ob}$ around the boundary $C$. It is given by

$$\Gamma_{ob} = \oint_C V_R dR \ . \qquad (3.4)$$

Thus, the so-called "cell circulation" $\Gamma_{ob}$ around the $i, k$ grid cell, assigned to the midpoint of each cell for plotting purposes, is

$$\begin{aligned}\left(d\Gamma_{i+1/2,k+1/2}\right)_{ob} = \frac{\Delta R}{2}[&V_R(R_i, \alpha_o', \beta_{k+1}) \\ &+V_R(R_{i+1}, \alpha_o', \beta_{k+1}) - V_R(R_{i+1}, \alpha_o', \beta_k) \\ &-V_R(R_i, \alpha_o', \beta_k)] \ , \qquad (3.5)\end{aligned}$$

where $i$ is the index in the range direction, $k$ is the index in the azimuth direction, and $\Delta R = R_{i+1} - R_i$ is the range increment. Circulation is additive (Petterssen 1956, p. 127; Hess 1959, p. 210). Thus, the circulation around the outer perimeter of a union of contiguous grid cells is simply the sum of the circulations around the perimeter of each grid cell.

## 4. AREAL EXPANSION RATE AND DIVERGENCE

In a manner analogous to the development of Eq. (3.1), we consider a two-dimensional (2D) velocity field so that Green's theorem is equivalent to the 2D version of the divergence theorem. By definition, the rate of expansion of the area enclosed by a closed circuit $C$ is the line integral around the circuit of the radial component of vector velocity $\mathbf{V}$, and is equivalent to the integral over the corresponding area $A$ of the component of divergence in the fluid surface. Thus, by the divergence theorem, the relationship between areal expansion rate and horizontal divergence is given by

$$\frac{dA}{dt} \equiv \dot{A} = \oint_C \mathbf{V} \cdot d\mathbf{n} = \iint_A \left(\boldsymbol{\nabla}_{\alpha_o'} \cdot \mathbf{V}\right) dA \ , \qquad (4.1)$$

where the overdot on $\dot{A}$ denotes differentiation with respect to time $t$ and $\boldsymbol{\nabla}_{\alpha_o'}$ is the gradient operator with $\alpha_o'$ held constant.

In radar spherical coordinate system, the element of area $dA$ (Hildebrand 1962, p. 304) on the $\alpha_o'$-surface in Eq. (4.1) is

$$dA = \cos\alpha_o' R\ dR\ d\beta \ , \qquad (4.2)$$

where the area of the $i, k$ grid cell is given as

$$A_{i+1/2,k+1/2} = \frac{1}{2}\cos\alpha_o'\left(R_{i+1}^2 - R_i^2\right)(\beta_{k+1} - \beta_k) \ , (4.3)$$

where $A_{i+1/2,k+1/2}$ is computed at the midpoint of each cell. Let $R_h = R\cos\alpha_o'$ be the horizontal range, $A$ be the signed area enclosed by a curve $C$ in the $\alpha_o'$-surface, and $A_o = A\cos\alpha_o'$ and $C_o$ be the projections of $A$ and $C$ onto a horizontal plane. Using the formula for the area of a plane region in polar coordinates (Kreyszig 1972, p. 339), we have

$$A_o = -\frac{1}{2}\oint_{C_o} R_h^2 d\beta \ , \qquad (4.3)$$

where $A_o$ is positive when $C_o$ is traversed counterclockwise. Hence,

$$A = -\frac{1}{2}\cos\alpha_o' \oint_C R^2 d\beta \ . \qquad (4.4)$$

The minus signs in Eqs. (4.3) and (4.4) arise because $\beta$ increases in the clockwise direction.

Differentiating Eq. (4.4) with respect to time $t$ and integrating by parts gives the rate of areal expansion on the $\alpha_o'$-surface, via $V_R = R_t$ and $V_\beta = R\cos\alpha_o'\,\beta_t$ calculated from Eq. (2.2),

$$\dot{A} = -\cos\alpha_o' \oint_C V_R R d\beta + \oint_C V_\beta dR \ , \qquad (4.5)$$

where the first and second terms on the right-hand side of Eq. (4.5) are the observed and unobserved effluxes, respectively. When $V_\beta$ is ignored in this equation, we obtain the observed areal expansion rate around the boundary $C$ because only one velocity component, $V_R$, is observed. The so-called "cell areal expansion rate" in Eq. (4.5) represents the observed ($ob$) expansion rate of the $i, k$ grid cell calculated at the midpoint of the cell and is therefore obtained by

$$\left(\dot{A}_{i+1/2,k+1/2}\right)_{ob} = \frac{1}{2}\cos\alpha_o' \left(\beta_{k+1} - \beta_k\right) \times \{R_{i+1}[V_R(R_{i+1},\alpha_o',\beta_{k+1}) + V_R(R_{i+1},\alpha_o',\beta_k)] - R_i[V_R(R_i,\alpha_o',\beta_{k+1}) + V_R(R_i,\alpha_o',\beta_k)]\}\ . \qquad (4.6)$$

In Eq. (4.6), the observed areal expansion rate of a union of contiguous grid cells is the sum of the areal expansion rates of the individual cells.

## 5. HIGH-RESOLUTION NUMERICAL MODEL

A "truth" tornadic supercell simulation was generated using version 3.6.1 of the Advanced Research Weather Research and Forecasting (WRF-ARW) model (Skamarock et al. 2008) with 111-m horizontal grid spacing and typical cloud model settings. The 111-m grid was run concurrently within a 333-m simulation in a one-way nested configuration. The 333-m simulation was initialized using a thermal bubble and the Rapid Update Cycle (RUC; Benjamin et al. 2004) sounding valid near the 24 May 2011 El Reno, Oklahoma tornadic supercell. The evolution of the 333-m supercell simulation was described in Potvin et al. (2017). The nested 111-m simulation was initialized 30 min into the 333-m simulation, at which time a mature supercell is present. Overall, the simulation lasted 150 min. The 333-m and 111-m grids used time steps of 1 s and 1/3 s, respectively, and a 50-level stretched vertical grid with spacing increasing from ~100 m near the surface to ~600 m between 10 km and 22 km AGL (model top). The simulation was carried out until 9000 s. The Thompson microphysics scheme (Thompson et al. 2004, 2008), which used five hydrometeor categories and predicted two moments of the rain and cloud ice particle size distributions, was used. Turbulence was parameterized using the 1.5-order turbulence kinetic energy (TKE) closure. Radiation was neglected for simplicity. A free-slip lower boundary condition was used, effectively disregarding the effects of surface drag. The lateral boundaries of the 333-m (parent) grid were open; the lateral boundaries of the 111-m nested grid were interpolated from the 333-m grid at each model time step. A Rayleigh damping layer was used at the model top to mitigate reflection of gravity waves off the model top. Centrifuging of raindrops, which produces a low-reflectivity eye inside a tornado-like vortex core region and a high-reflectivity annulus outside the core region (Dowell et al. 2005), was not simulated due to the coarse model resolution.

The supercell simulation will be used to assess estimates of low-level supercell circulation and areal expansion rate diagnosed from virtual Doppler radar data. This will be shown in subsequent sections.

## 6. WSR-88D RADAR EMULATOR

Doppler velocity and reflectivity measurements of the simulated low-level supercell rotation embedded in a low-level convergent flow were produced by scanning a virtual Doppler radar across the 3-D gridded data of eastward ($u$), northward ($v$) and vertical ($w$) components of flow, terminal velocity ($V_T$), and radar reflectivity ($dBZ$). Data were trilinearly interpolated to a radar point within a beamwidth volume. The Doppler radar emulator reproduced the basic characteristics of a WSR-88D. Several simplifications, however, were employed. Instead of the radar beam consisting of a main lobe and sidelobes, it consisted only of a main lobe that was represented by a Gaussian distribution. The width of the beam typically is specified by the half-power beamwidth, which is the angular width of the beam where the power was one-half of the peak power at the center of the beam. The range and azimuth spacings are 250 m and 1.0°, respectively.

In reality, WSR-88D Doppler velocity measurements include errors that have a standard deviation of about 1.0 m s$^{-1}$. In our simulations, this uncertainty was included by adding Gaussian-distributed random noise to non-missing Doppler velocity and reflectivity values.

We assume that simulated radial velocity data have been dealiased (e.g., Jing and Wiener 1993) and that simulated reflectivity data have been quality-controlled to eliminate the nonmeteorological radar echoes such as biological returns (bats, birds, insects), anomalous propagation, instrument artifacts, and ground clutter (e.g., Lakshmanan et al. 2014).

## 7. SIMULATION RESULTS

The evolution of a supercell producing two tornado-like vortices (hereafter, "tornadoes") is portrayed in Figs. 1-3. Fig. 1 illustrates evolving low-level reflectivity fields at (a) t=0 min, (b) t=40 min, and (c) t=90 min into the simulations. The nested 111-m simulation was initialized 30 min into the 333-m simulation, at which time a young supercell storm was present (Fig. 1a). A hook echo grew as the first tornado developed ~80 min into the simulation (Figs. 1b and 1c) and became very intense with surface winds (not shown) briefly exceeding 110 m s$^{-1}$ and a strong updraft ($w$) surpassing 80 m s$^{-1}$ (Fig. 2) at low altitudes.

There are several cycles of maximum vertical velocity ($W_{max}$, Fig. 2), suggesting pulsating updrafts near storm top and near ground at different times. The updraft pulsations aloft are not reflected at low altitudes. There are six low-level updraft maxima below the 2.0-km height at *t* = 90, 113, 125 130 and 140 min (Fig. 2), whereas numerous upper-level updraft maxima occur around the 10-km height. At low altitudes, updraft intensification is closely associated with low-level vertical vorticity intensification (Fig. 3). Wicker and Wilhelmson (1995) discussed updraft intensification mechanisms and pulsations.

Figures 4 and 5 present the plots of (a) radar reflectivity, (b) ground-relative Doppler velocity, (c) cell circulation, and (d) cell areal expansion rate at the lowest elevation angle of 0.5º and at t = 40 and 90 min, respectively. The grid size in the figures is 10 km x 10 km, which has been enlarged from the small square shown in Figs. 1b and 1c.

Since the Doppler radar senses only the component of flow in the radar viewing direction, zero Doppler velocity (gray area) indicates flow that is entirely perpendicular to the viewing direction (Fig. 4b). The red (green) area represents outbound (inbound) velocities relative to the radar. The Doppler velocity signature indicates a combination of strong convergence and weak cyclonic rotation associated with strong inflow spiraling cyclonically toward the center of the updraft base before turning up within the updraft. This is a prominent feature of the organizing stage of a supercell.

Cell circulation values are computed and plotted (Fig. 4c), corresponding to the Doppler velocity field (Fig. 4b) at *t* = 40 min. A band of high cell circulations is situated nearly along the zero Doppler velocity band. Figure 4d shows a band of high areal contraction rate situated along the edge of a nascent hook echo (delineated by the zero dBZ contour in Figs. 1b and 4a) at *t* = 40 min. This is indicative of strong, low-level inflow toward the center of the updraft base (Fig. 4b).

Searching for and detecting some significant features of circulation and areal expansion rate outside the zero dBZ contours (e.g., Fig. 4) is problematic. This is because Doppler velocity data with corresponding reflectivity values at or below 0 dBZ in the WSR-88Ds are not always available for automatically detecting cell circulation and cell areal expansion rate values during the nascent stage of a severe storm.

Plots of radar reflectivity, ground-relative Doppler velocity, cell circulation and cell areal expansion rate at the lowest elevation angle of 0.5º and at t = 90 min are presented in Fig. 5. A well-pronounced hook echo matured as the first simulated tornado (T1) developed ~80 min into the simulation and became very intense with a strong updraft surpassing 80 m s$^{-1}$ (Fig. 2) and high vertical vorticity exceeding 1.0 s$^{-1}$ (Fig. 3) at low altitudes.

Calculated cell circulation and cell areal expansion rate values at t = 90 min are, respectively, found to be 11.1 x 10$^3$ m$^2$ s$^{-1}$ (Fig. 5c) and -9.9 x 10$^3$ m$^2$ s$^{-1}$ (Fig. 5d). The measured values have increased in magnitude from those at t = 40 min (Fig. 4). Increased values of cell circulation and areal contraction rate may give an early warning of imminent tornadogenesis.

The salient feature in Fig. 5d is the extreme negative values of cell areal expansion rate situated at the approximate center between the extreme positive and negative Doppler velocity values, implying a strong localized convergence at low levels (indicated by two orange arrows pointing toward each other on the Doppler velocity pattern). It indicates that a narrow, strong updraft (Fig. 2) within the simulated first tornado (indicated by T1 in Fig. 3).

Fig. 6 portrays time series of maximum cell circulation $(\Gamma_{ob})_{max}$ and minimum cell areal expansion rate $(\dot{A}_{ob})_{min}$ at lowest elevation angle ($\alpha_o'$) of 0.5° and approximately 50-km range and 325° azimuth from Doppler radar. For comparison, the quantitative evolutions of low-level maximum vertical vorticity ($\zeta_{max} = v_x - u_y$), minimum horizontal divergence ($\delta_{min} = u_x + v_y$), and vertical velocity maximum ($W_{max}$) within the 130-minute supercell simulation are plotted. Overall, the $(\Gamma_{ob})_{max}$ and $(\dot{A}_{ob})_{min}$ time series compare qualitatively well to the numerical time series of $\zeta_{max}$ and $\delta_{min}$, respectively.

## 8. CONCLUSIONS AND FUTURE WORK

A "truth" tornadic supercell simulation was generated using the high-resolution WRF-ARW model. The simulation was conducted to assess estimates of simulated low-level supercell $\Gamma_{ob}$ and $\dot{A}_{ob}$ diagnosed from virtual Doppler velocity signatures of rotation and convergence at low altitudes and close radar. The estimates compared qualitatively well to the numerical model results.

We will continue this work by constructing Hovmöller diagrams to highlight the roles of simulated $\Gamma_{ob}$ and $\dot{A}_{ob}$ estimates and also the effects of range and azimuth on simulated $\Gamma_{ob}$ and $\dot{A}_{ob}$ calculations. Furthermore, we will compute the $\Gamma_{ob}$ and $\dot{A}_{ob}$ values around "circles" of various radii approximately centered on Doppler convergent vortex signature centers by bilinearly interpolating data to judiciously chosen points on the circles and using a line-integral method.

*Acknowledgments.* The authors thank Terry Schuur of NSSL for providing his helpful comments.

## 9. REFERENCES


Benjamin, S. G., and Coauthors, 2004: An hourly assimilation–forecast cycle: The RUC. *Mon. Wea. Rev.*, **132**, 495–518, doi: 10.1175/1520-0493(2004)132<0495:AHACTR>2.0.CO;2.

Doviak, R. J., and D. S. Zrnić, 1993: *Doppler Radar and Weather Observations.* 2nd ed. Academic Press, 562 pp.

Dowell, D. C., C. R. Alexander, J. M. Wurman, and L. J. Wicker, 2005: Centrifuging of hydrometeors and debris in tornadoes: Radar-reflectivity patterns and wind-measurement errors. *Mon. Wea. Rev.*, **133**, 1501-1524.

Hess, S. L., 1959: *Introduction to Theoretical Meteorology.* Holt, Rinehart and Winston, 362 pp.

Hildebrand, F. B., 1962: *Advanced Calculus for Applications*, Prentice-Hall, 646 pp.

Jing, Z., and G. Wiener, 1993: Two-dimensional dealiasing of Doppler velocities. *J. Atmos. Oceanic Technol.,* **10**, 798-808, doi:10.1175/1520-0426(1993)0102.0.CO;2.

Kreyszig, E., 1972: *Advanced Engineering Mathematics* (3rd ed.), Wiley, 866 pp.

Lakshmanan, V., C. Karstens, J. Krause, and L. Tang, 2014: Quality control of weather radar data using polarimetric variables. *J. Atmos. Oceanic Technol*., **31**, 1234–1249, doi:10.1175/JTECH-D-13-00073.1.

Petterssen, S., 1956: *Weather Analysis and Forecasting, Vol. I, 2nd ed.,* New York, McGraw-Hill Book Co. Inc., 428 pp.

Potvin, C. K., E. M. Murillo, M. L. Flora, and D. M. Wheatley, 2017: Sensitivity of supercell simulations to initial-condition resolution. *J. Atmos. Sci.*, **74**, 5-26, doi: 10.1175/JAS-D-16-0098.1.

Skamarock, W. C., and Coauthors, 2008: A description of the Advanced Research WRF version 3. NCAR Tech. Note NCAR/TN-475+STR, 113 pp., doi:10.5065/D68S4MVH.

Thompson, G., R. M. Rasmussen, and K. Manning, 2004: Explicit forecasts of winter precipitation using an improved bulk microphysics scheme. Part I: Description and sensitivity analysis. *Mon. Wea. Rev.*, **132**, 519–542, doi:10.1175/1520-493(2004)132<0519:EFOWPU>2.0.CO;2.

Thompson, G., P. R. Field, R. M. Rasmussen, and W. R. Hall, 2008: Explicit forecasts of winter precipitation using an improved bulk microphysics scheme. Part II: Implementation of a new snow parameterization. *Mon. Wea. Rev.*, **136**, 5095–5115, doi:10.1175/2008MWR2387.1.

Wicker, L. J., and R. B. Wilhelmson, 1995: Simulation and analysis of tornado development and decay with a three-dimensional supercell thunderstorm. *J. Atmos. Sci.,* **52,** 2675-2703.

Wood, V. T., and R. P. Davies-Jones, 2015: Circulation and areal contraction rate as detected and measured by Doppler radar. Extended abstracts, *37th Conference on Radar Meteorology*, Norman, OK, Amer. Meteor. Soc., P103.

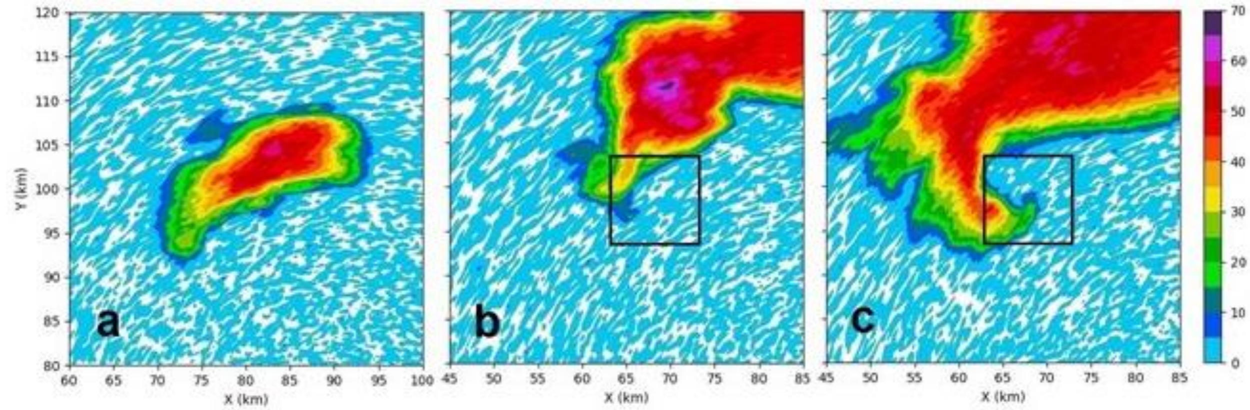


*Fig. 1. Illustration of evolving low-level reflectivity fields at (a) t=0 min, (b) t=40 min, and (c) t=90 min into the simulations. The size of the large grid is 40 x 40 km; a small grid size of 10 x 10 km is indicated by a smaller square. This square will be enlarged for examining the simulated signatures of Doppler velocity and reflectivity and also signatures of cell circulation and cell areal expansion rate.*

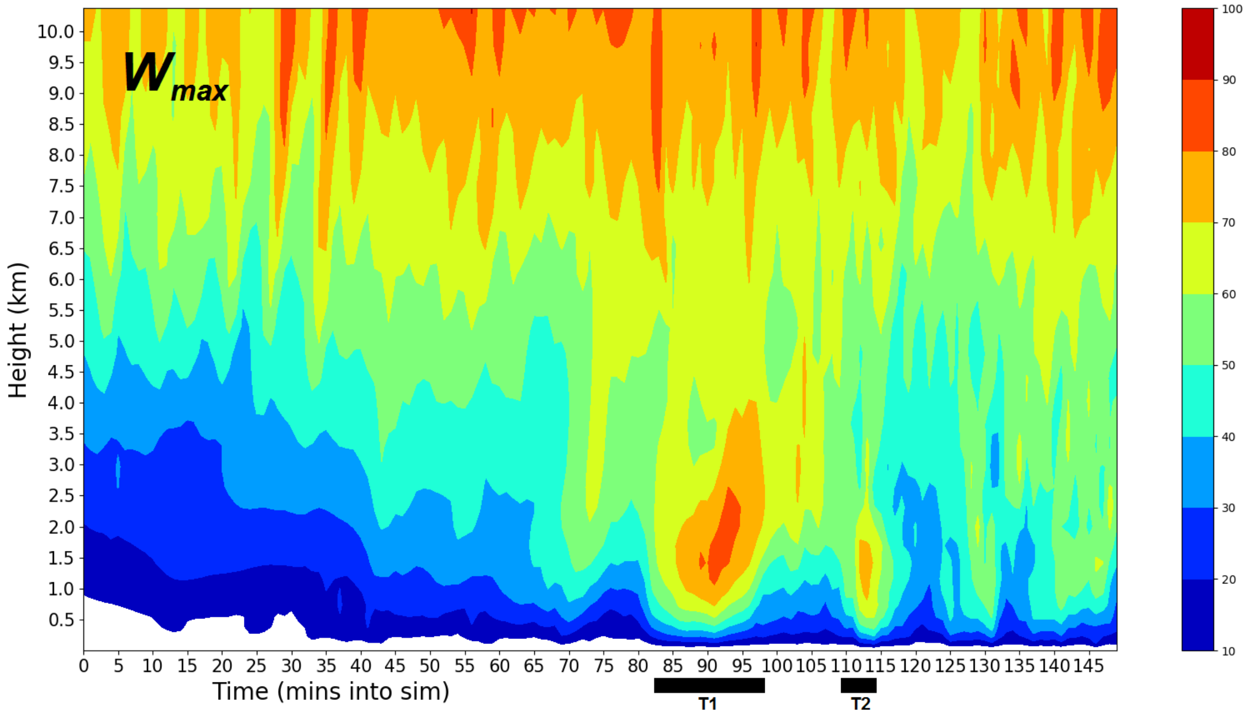


*FIG. 2. Height-time plot of the numerical vertical velocity ($W_{max}$, m s$^{-1}$) peaks. Black rectangles represent durations of two simulated tornadoes, as indicated by T1 and T2. Near the ground, a white shading refers to 0 < $w$ < 10 m s$^{-1}$.*

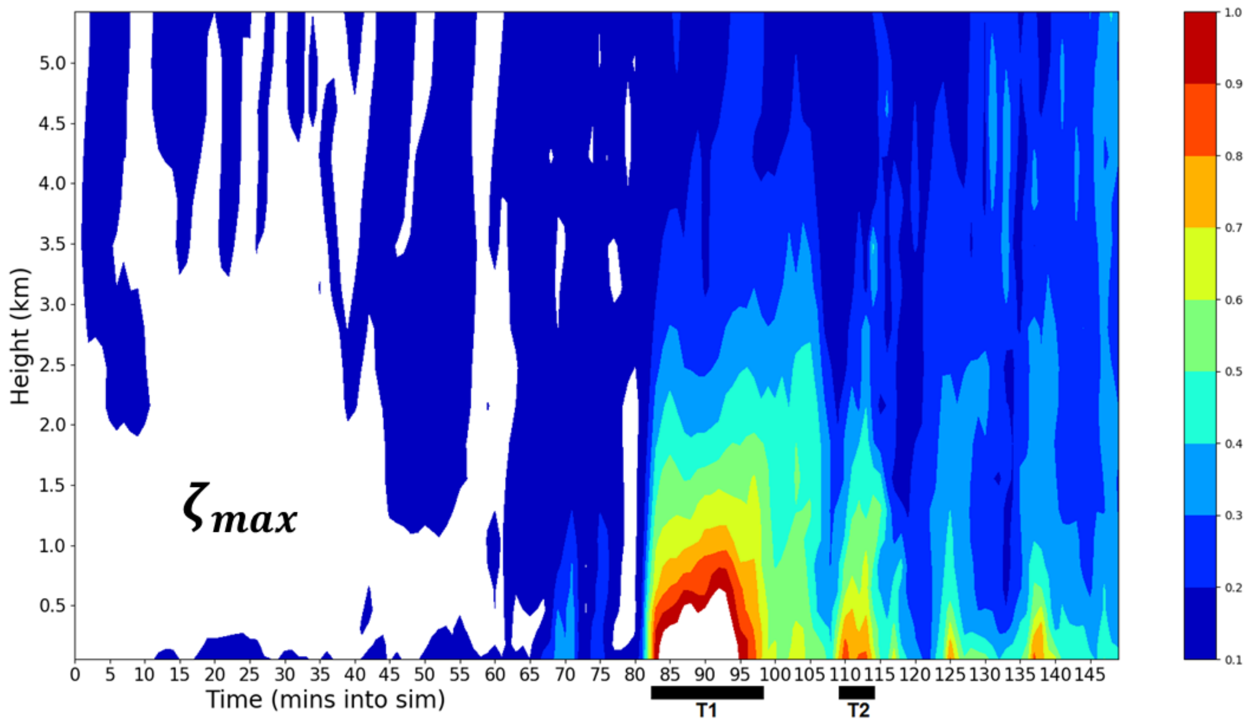


*FIG. 3. Height-time plot of the numerical vertical vorticity ($\zeta_{max}$, $s^{-1}$) peaks. Black rectangles represent durations of two simulated tornadoes, as indicated by T1 and T2. A white shading inside a dark red shading refers to $\zeta_{max}$ > 1 $s^{-1}$, while at the same time, another white shading surrounded by a dark blue shading refers to $0 < \zeta_{max} < 0.1$ $s^{-1}$. The vorticity peak within the white shading is 1.3 $s^{-1}$. Note that height is reduced to about 5 km AGL (comparing to that in Fig. 2) to enlarge the detailed vorticity field near the ground.*

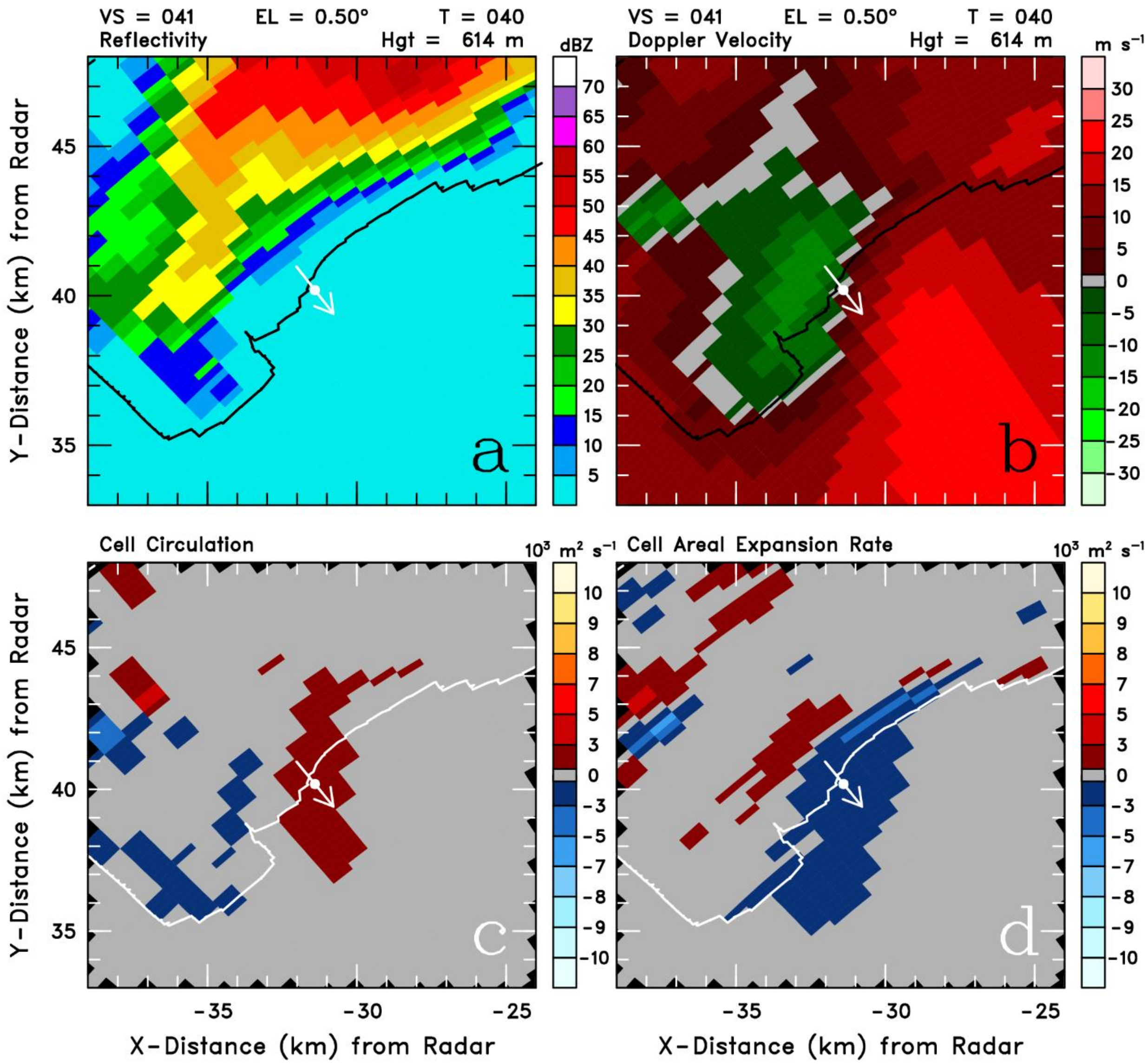


*Fig. 4. Plots of (a) radar reflectivity (dBZ), (b) ground-relative Doppler velocity (m s$^{-1}$), (c) cell circulation ($\Gamma_{ob}$, 10$^3$ m$^2$ s$^{-1}$), and (d) cell areal expansion rate ($\dot{A}_{ob}$, 10$^3$ m$^2$ s$^{-1}$) at the lowest elevation angle of 0.5º and at t = 40 min. In (b), the red (green) grids represent positive (negative) Doppler velocities away from (toward) the radar. The gray zero Doppler velocity band represents flow perpendicular to the radar viewing direction. The zero dBZ contours are indicated by white and black contours in all panels. The approximate center of the 10 km x 10 km grid (black squares in Figs. 1b and 1c) is indicated by a white dot on the midpoint of a white arrow pointing to the radar. That dot represents the height (Hgt, m) of the radar beam. VS stands for the radar's volume scan number. Tick marks are separated by 1 km.*

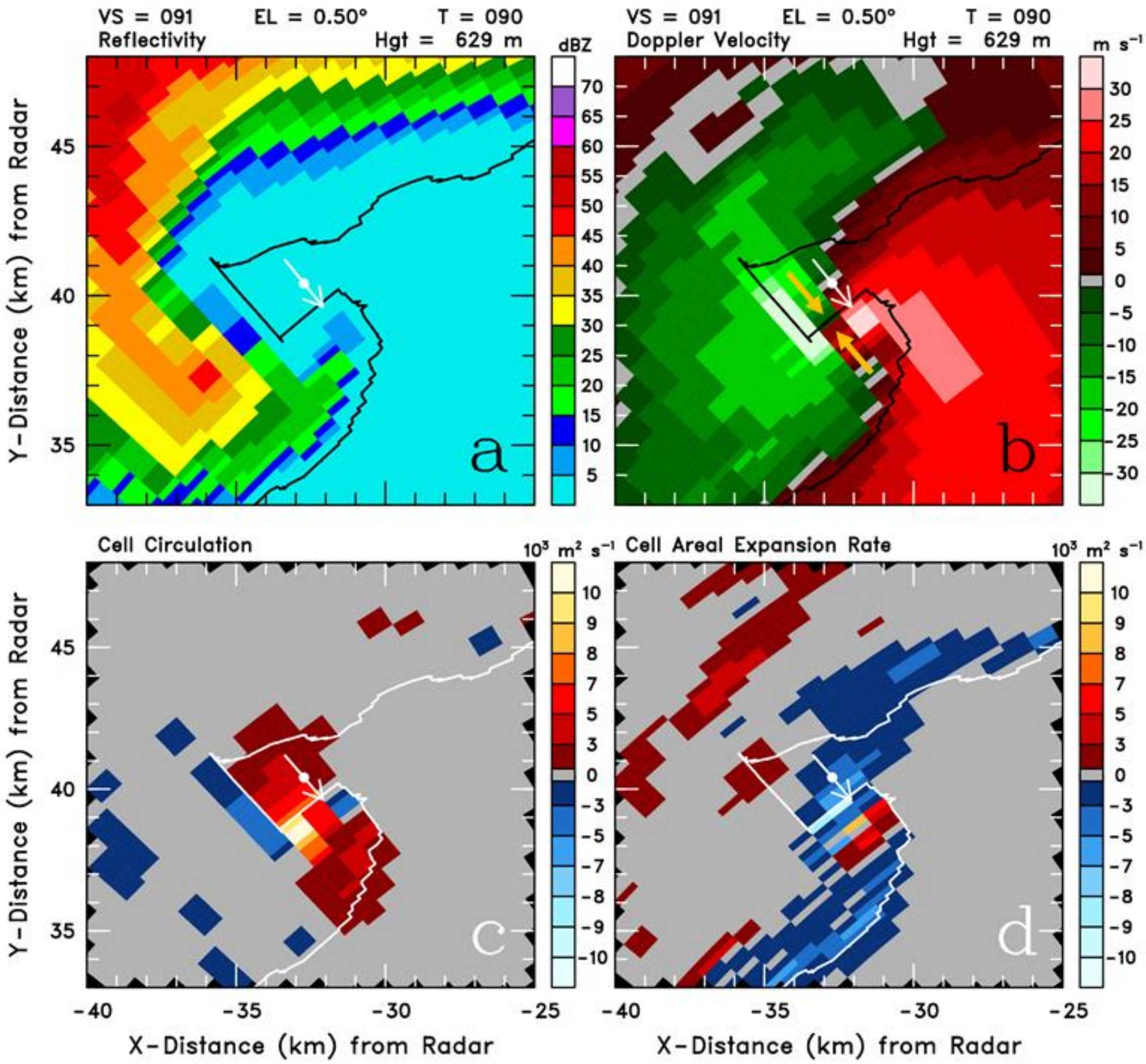


*Fig. 5. Same as Fig. 4, except at t = 90 min. In (b), two orange arrows represent flow toward and away from the radar measured along the radar viewing direction that passes through the Doppler vortex signature center.*

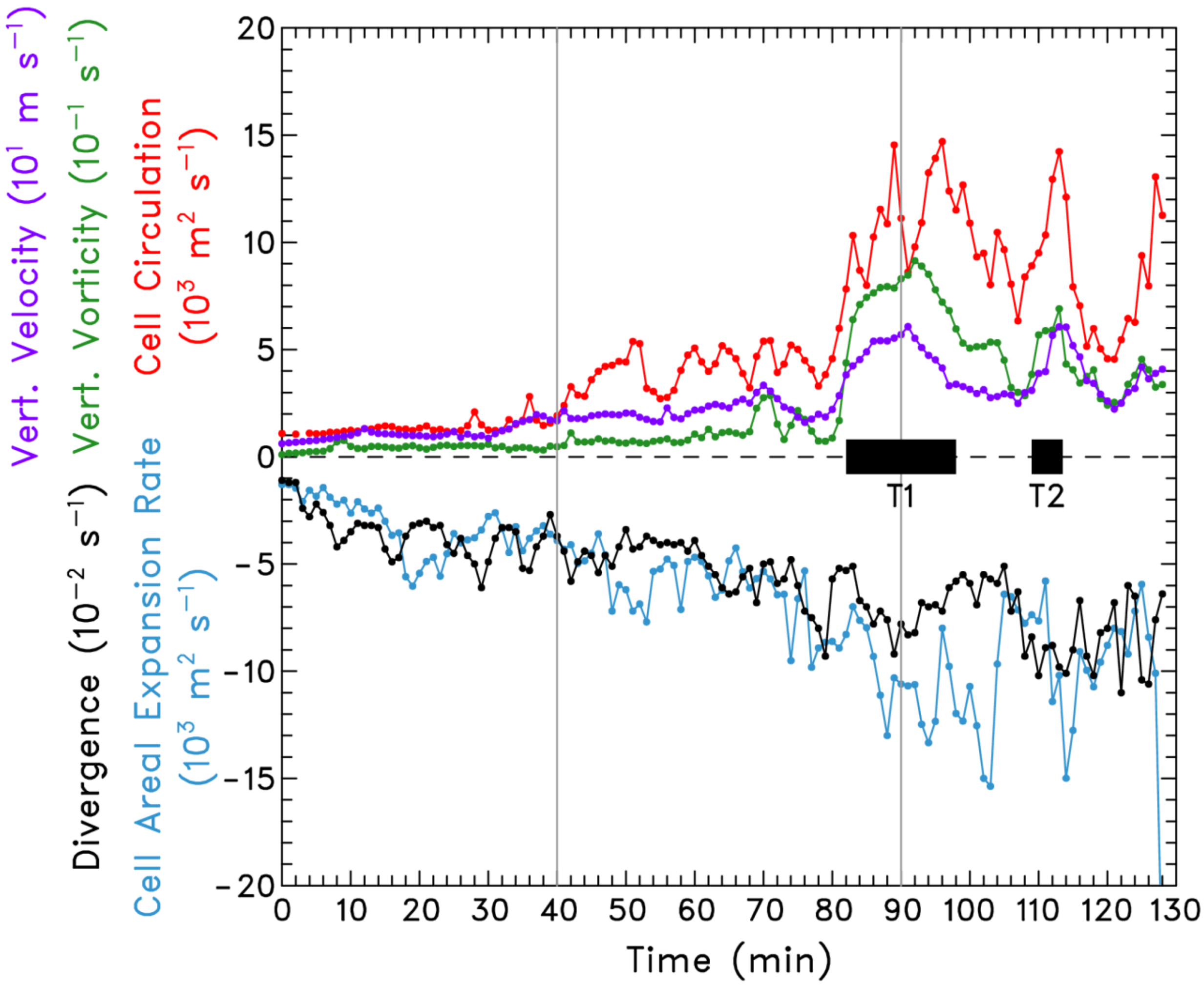


*Fig. 6. Time series of low-level values of maximum $\Gamma_{ob}$ (red dotted curve) and maximum $\dot{A}_{ob}$ (blue dotted curve) at lowest elevation angle of 0.5° and approximately 50-km range and 325° azimuth from Doppler radar. Profiles are valid at approximately 550 m AGL. Time series of low-level numerical values of $\zeta_{max}$ (green dotted curve), $\delta_{max}$ (black dotted curve), and $W_{max}$ (magenta dotted curve) are plotted for comparison to those of $\Gamma_{ob}$ and $\dot{A}_{ob}$. Data are separated by 1 min. The gray vertical lines occur at t=40 and 90 min, corresponding to Figs. 4 and 5. Black rectangles represent the durations of two simulated tornadoes (T1 and T2).*